Materials Research Express

PAPER

Laser surface modification of Mg-Zn-Gd alloy: microstructural, wettability and *in vitro* degradation aspects

To cite this article: Rakesh K R *et al* 2018 *Mater. Res. Express* **5** 126502

Materials Research Express

PAPER

Laser surface modification of Mg-Zn-Gd alloy: microstructural, wettability and *in vitro* degradation aspects

RECEIVED
4 June 2018

REVISED
27 August 2018

ACCEPTED FOR PUBLICATION
4 September 2018

PUBLISHED
19 September 2018

Rakesh K R[1], **Srikanth Bontha**[1,4], **Ramesh M R**[1], **Shashi Bhushan Arya**[1], **Mitun Das**[2], **Vamsi Krishna Balla**[2,4] **and Srinivasan A**[3]

[1] National Institute of Technology, Karnataka, Surathkal, 575025, India
[2] Bioceramics and Coating Division, CSIR-Central Glass and Ceramic Research Institute, 196 Raja S.C. Mullick Road, Kolkata700 032, West Bengal, India
[3] CSIR- National Institute for Interdisciplinary Science and Technology, Thiruvananthapuram, 695019, India
[4] Authors to whom any correspondence should be addressed

E-mail: srikanth.bonth@nitk.edu.in **and** vamsiballa@cgcri.res.in

Keywords: Mg-Zn-Gd, laser surface melting, wettability, *in vitro* degradation

Abstract

Mg-Zn-Gd have great potential for biomedical applications owing to excellent bioactivity and non-toxicity properties. In the present study, laser surface melting (LSM) was carried out on newly developed Mg-1Zn -2Gd (wt%) alloy. Effects of laser energy on microstructural evolution, corrosion properties, surface energy, and hardness have been investigated. The surface modified sample processed at different energy densities showed fine grain structure in the melt zone compared to the untreated substrate. Grain refinement in the laser melted region improved the hardness by 60%. The surface roughness was found to be increased with increasing laser energy density. At higher energy density, removal of materials from the surface is enhanced, resulting in deeper grooves and higher surface roughness. The wettability studies indicated that the variations in surface geometry, grain size and surface roughness of LSM samples strongly influence the surface energy and hydrophilicity. Improved wetting of LSM sample was achieved owing to grain refinement and low surface roughness. The corrosion resistance determined by immersion and electrochemical methods of laser melted sample in Hank's balanced salt solution improved considerably due to grain refinement, meltpool depth and uniform distribution of secondary phases.

1. Introduction

Common biomedical metallic materials (Ti-6Al-4V, Stainless steel, Co-Cr based alloys) have elastic moduli higher than that of human bone leading to stress shielding [1]. In the case of temporary implants fixations, these materials are not biodegradable and therefore require second surgery to remove them once the bone healing is complete. Therefore, magnesium (Mg) based metallic materials are being studied extensively as potential candidate materials for biodegradable temporary osseosynthetic implants. Since Mg based implants are resorbed by the body and their mechanical properties such as low density (1.7 g cm^{-3}), elastic modulus (41–45 GPa) are close to those of human bone, these alloys can became attractive since they addressed the drawbacks of existing metallic implant materials [2]. However, Mg alloys are electrochemically very active due to their low potential (−2.363 V versus SHE) and are prone to accelerated degradation in the physiological environment [3]. To overcome this, several research activities have been focused on alloy development and surface modifications. Among different magnesium alloys, Mg-Ca [4], AZ63 [5], AZ91D [6], WE43 [7], LAE442 [7], AZ31 [8] are few alloys that have been extensively studied for biomedical applications. From these studies it became known that the addition of rare earth elements (REE) to base Mg alloys has a profound influence on their mechanical and corrosion properties. Recent studies on Mg containing gadolinium (Gd) and other REE's revealed that the mechanical properties can be tailored via precipitation strengthening and considerable improvement *in vivo* corrosion performance can also be achieved [1]. Feyerabend *et al* [9] investigated *in vitro*

cytotoxicity of few REE's such as lanthanum (La), cerium (Ce), gadolinium (Gd), neodymium (Nd), dysprosium (Dy), yttrium (Y) and among these Gd and Dy are reported non-toxic (All together 3.4 wt% of REE) in nature. Zinc (Zn) is another important alloying element to Mg-REE alloys which can improve strength and toughness due to formation of Long Period Stacking Order (LPSO) phase combined with fine grained microstructures [10].

Since the corrosion resistance is essentially a surface dependent property, it can be controlled by tailoring the surface characteristics such as microstructure and near-surface chemical composition. Among different surface modification techniques such as ion implantation, friction stir processing, chemical passivation etc [11], laser surface melting (LSM) is very attractive due to its ability to modify the surface precisely and locally by tailoring laser energy. In LSM, the rapid heating and cooling rates would homogenize and refine the microstructures in a shallow melted region [12]. Furthermore the surface melting can also be used to dissolve secondary phases that would help in enhancing the corrosion resistance [13]. So far, some efforts have been made to understand the effect of LSM on corrosion performance of magnesium alloys [14]. Abbas *et al* studied [15] continuous wave CO_2 laser melting of AZ31, AZ61 and WE43, and reported that the improvement in corrosion resistance was mainly due to microstructural refinement and uniform distribution of corrosion resistant β phase. In case of AZ91D and AM60B processed by Nd:YAG laser the corrosion resistance was unaffected, but significant refinement of the microstructure has been recorded in both alloys [16]. Similarly, laser surface modification of AZ91D alloy was carried out using a high power diode laser and different microstructures were observed depending on the energy inputs. At low energy input selective melting of the surface resulted in modification of only one phase of the alloy and effective melting of phases was reported at high energy input. It was also observed that the depth of treatment was insensitive to scan speed at high laser power [17]. In another study, the corrosion rate of laser melted AZ91D was found to increase with increasing laser power and decreasing laser scanning speed [18]. However LSM of ZE41 did not show any improvement in the corrosion resistance [19]. A study on laser melting of MEZ alloy by Majumdar *et al* [20] showed significant improvement in the microhardness and pitting corrosion resistance.

For implant applications, surface characteristics of these alloys play an evident role in protein absorption and cell/osteoblast growth [21]. The quality and amount of cells that attach on to the surface are substantially influenced by the surface characteristics such as roughness, chemical composition, surface energy and compositional heterogeneity of the surface [22]. For example, nanoscale surface roughness of Ti was demonstrated to be very effective in enhancing osseo integration [23]. Osteoblast proliferation and differentiation as well as production of local growth factors are also influenced by surface roughness. Guan *et al* found that AZ31B alloy surface modified using femtosecond pulse laser irradiation causes micro and nano ripples. The combined effect of surface roughness and interference of laser leads to the surface topographical changes in the alloy [24]. Use of ns-pulsed fiber laser for surface melting of AZ31B alloy led to changes in surface roughness as well as mechanical properties. It is concluded that control in laser process parameters allows changes in surface roughness values (Ra). Surfaces with monodirectional, homogenous and nano fibrous structure were observed after melting [25]. Wettability is another important surface property that dictates biological interaction through cell adhesion on the surface [26]. The nature of the water contact angle on laser surface textured AZ31, with cauliflower type of surface roughness, were found to be hydrophilic and is mainly attributed to the surface topography and chemistry [27]. Surface energy is generally directly related to the wettability of a surface [22]. The materials with high wettability/surface energy (hydrophilicity) promote rapid cell adhesion, growth and better biocompatibility [28]. Therefore, the surface wettability of an implant material helps in estimating the overall cell-materials interactions and long term or short term stability [29]. The results showed that laser treatment is a promising technique for tailoring biodegradation behavior and wettability of Mg alloys by changing the surface structure [30]. In this context, laser surface modification is very efficient for phase modification, grain refinement on the surface without changing the bulk properties of the material [31]. The present work is aimed at understanding the influence of laser surface melting (LSM) of Mg-1Zn-2Gd (wt%) alloy on microstructures and *in vitro* wettability and degradation. LSM processing was carried out using Optomec MR-7 System. The effect of laser energy density on surface characteristics of treated samples was investigated by changing the laser power and scan velocity. The changes in the surface characteristics such as microstructure and roughness were correlated with wettability, degradation and hardness of Mg-1Zn-2Gd alloy. The cytotoxicity study of the prepared alloy was carried out and the result proven that there is no adverse effect caused by this alloy on cells (This paper is in the process of publication).

2. Materials and methods

2.1. Preparation of alloy and laser surface melting

Mg-1Zn-2Gd (wt%) alloy was prepared by conventional casting route which was performed in a mild steel crucible under protective atmosphere (Ar+2%SF_6). Initially Mg-Zn melt was prepared followed by addition of

Table 1. Typical composition of laser treated zone and as cast Mg-Zn-Gd alloys analyzed by EDS (wt%).

Sample conditions (Within the grain)	Mg	Zn	Gd
As cast alloy	96.9 ± 0.8	1.2 ± 0.4	1.7 ± 0.6
12.5 J mm^{-2}	95.8 ± 0.5	1.8 ± 0.6	2 ± 0.8
45 J mm^{-2}	94.7 ± 0.5	2.2 ± 0.8	2.8 ± 0.6

required amount of Gd (99.9% pure, Metal Industries, Mumbai) at 750 °C. Zr of 0.8 wt% was also added to the molten pool for grain refinement. Then the melt was held for 20 min, to achieve complete dissolution of the alloying elements, and stirred for 2 min. The stirred melt was then poured into a preheated (250 °C) cast iron mould (200 mm × 110 mm × 20 mm). The elemental composition of the cast alloy was determined using Inductively Coupled Plasma-Atomic Emission spectroscopy (ICP-AES) (IRIS INTREPID II XSP DUO, Thermo Electron, Australia) and the composition found to be for the prepared alloy is Mg-1%Zn-2%Gd (wt%).

The cast Mg-Zn-Gd alloy block was cut into smaller pieces (100 mm × 30 mm × 8 mm) and one surface with 90 mm × 20 mm area was used for laser surface melting (LSM). The sample surface were ground using SiC abrasive papers ranging from grade 220 to 2000 (grit size). LSM was carried out using MR-7 equipment from Optomec Inc., USA. LSM was carried out in high purity argon purged glove box with oxygen content less than 10 ppm. A continuous wave Ytterbium doped fiber laser with beam diameter of 500 μm was used for LSM. The focal position is approximately 1 mm below the surface of the sample. Different laser powers (125, 175, 225 W) were used at scan velocities of 10 and 20 mm s^{-1} to achieve different laser energy densities (12.5, 17.5, 22.5, 25, 35, 45 J mm^{-2}). The energy density was calculated as $E = P/\nu.d$, where P is laser power (W), ν is scan velocity (mm s^{-1}) and d is laser beam diameter (500 μm). The distance between two successive laser scans was maintained at 0.5 mm. The laser processing conditions were marked as power and scan speed (i.e., 225 W power and 10 mm s^{-1} velocity) represented as 225/10 in the following explanation. Table 1 shows the composition of the processed samples.

2.2. Microstructures, phase constituents, roughness and wettability

The cross section of the LSM samples was ground with emery paper of various grades (300 to 2000) followed by velvet cloth polishing with diamond paste. The polished surfaces were etched using acetic picrol for microstructural observation. The cross sectional microstructures and melt pool depth were analyzed using field emission scanning electron microscopy (SEM) in conjunction with energy dispersive spectroscopy (EDS) (CARL ZEISS, FESEM, Germany). The formation of different phases in the LSM regions was identified by glancing incident x-ray diffractometry (GIXRD) (Rigaku smart lab, Japan) operating at a voltage of 40 kV and current of 30 mA. The data was collected using a monochromatic CuK_α radiation ($\lambda = 0.154$ nm) with a scan speed of 2° per minute, step size of 0.02° and over a range of 40 to 80°. The micro hardness measurements were carried out on polished surfaces of the alloys using Vickers micro hardness tester (HMV-G20 Shimadzu, Japan). The applied load was 25 g with a dwell time of 15 s and an average of 10 measurements on each sample was reported.

Non-contact laser profilometer (OLYMPUS-LEXT 3D laser measuring microscope, OLS4000, Japan) was used to measure the surface roughness of laser treated and untreated alloys in terms of S_q (root mean square height, μm) and S_a (arithmetic mean height, μm). A minimum of three positions on each laser melted surface with 1 cm^2 area was scanned. Sessile drop technique was used to measure the surface wettability of Mg-1Zn-2Gd (wt%) alloy in LSM and polished condition. One set of LSM samples were polished to eliminate the effect of surface roughness on wettability. All samples were pre-cleaned by ultra-sonication in alcohol bath. Polar liquid (DI water) and non-polar liquid (Diidomethane) were used to determine the surface energy of the surface using contact angle measurement by dropping 1 μL volume of liquid onto the surface of the laser melted and polished samples. The angle formed between the droplet of liquid and the surface of the sample was captured by the camera attached with the goniometer. The surface energy of the sample was calculated by using Fowkes equation [32].

2.3. *In vitro* degradation behavior

In vitro degradation/corrosion behavior of LSM samples was measured using immersion and electrochemical methods. In immersion corrosion study, weight loss and hydrogen evolution measurements were performed. All LSM samples were ground with 2000 grit paper followed by fine polishing on velvet cloth to eliminate the surface roughness effect on corrosion measurements. A standard inverted funnel and burette set up proposed by Song *et al* [33] was used for this study. Static long term immersion study was carried out in 300 ml Hanks

balanced salt solution (HBSS) (HIMEDIA Labs, Bangalore) with initial pH of 7.4. All samples were encapsulated in a resin mould with LSM surface (1 cm^2) exposed to the HBSS for a period of 180 h at room temperature. The amount of hydrogen evolution was measured at every 12 h of immersion time and 10 ml of HBSS were used to analyze Mg ion release using atomic absorption spectrometer (932 Plus, GBC Scientific Equipment Ltd). No makeup solution added during the total period of immersion. After immersion, the degradation products from the surface of the samples were cleaned with a solution containing chromic acid (200 g L^{-1}) and silver nitrate (10 g L^{-1}). Then the samples were cleaned with distilled water and ethanol followed by drying in warm flowing air. The initial and final masses of the samples were measured using a four-digit precision balance. The degradation rate was calculated using the following relation[ASTM G31-72] [34].

$$(C.R)_w = \frac{(8.76) \times 10^4 \times W}{D \times A \times T} \quad (1)$$

where $(C.R)_w$ is the corrosion rate (mm/year or mmpy), W is the change in mass between initial and final condition (g), A is the exposed area (cm^2), D is the density of the material (g/cm^3) and T is the time in hours (h). The characteristics of degradation products and the surface features of the samples after corrosion were examined using SEM/EDS and XRD.

The electrochemical measurements on as-cast and LSM samples were carried out using an electrochemical workstation (EC Lab-Biologic, SP-150, France.) at room temperature. The set up consisted of saturated calomel electrode (SCE) as a reference electrode, a platinum wire as counter electrode and test samples as working electrode (1 cm^2). To understand the current response with applied potential a linear polarization study was performed at 100 mV above and below the corrosion potential at a scan rate of 0.5 mV s^{-1}. The corrosion current (i_{corr}) of the samples was determined using Tafel extrapolation, which was used to estimate the corrosion rate of the samples using following relation [ASTM G102-89].

$$(C.R)_i = \frac{K1.\ i_{corr}.EW}{\rho} \quad (2)$$

where $(C.R)_i$ is rrosion rate in mm/year or (mmpy), i_{corr} is corrosion current density in $\mu A\ cm^2$, EW is the equivalent mass of metal being tested and ρ is the density of the alloy in g/cm^3. The constant K1 is 3.27×10^{-3} mm g $(\mu A)^{-1}\ cm^{-1}\ y^{-1}$.

3. Results and discussion

3.1. Microstructural and phase analysis

Figures 1 and 2 show typical cross sectional microstructures of LSM Mg-Zn-Gd alloy processed at different energy density conditions. Significant changes of the microstructures were observed in the LSM zone compared to the untreated substrate. LSM is characterized by rapid heating and cooling rates, which resulted in noticeable refinement in the microstructural features of melted region compared to the substrate. The microstructure of cast Mg-Zn-Gd alloy typically consist of α-Mg dendrites (marked A in figure 2(a)), a eutectic mixture of α-Mg and LPSO phases (marked B in figure 2(a)) and $MgZn_2/Mg_7Zn_3$ [35] intermetallic phases. The semi-elliptical region marked in figure 2(b) is the laser-melted region. The depth of this melted region increased from 75 μm to 150 μm with increasing laser energy input (table 2, figure 1). In addition the melt depth increased with the increasing laser power and decreasing scan velocity. A minimum depth of 75 μm was observed at 125 W, 20 mm s^{-1} (12.5 J mm^{-2}) and maximum depth of 150 μm was recorded at 225 W, 10 mm s^{-1} (45 J mm^{-2}). The depth of the melted region can potentially have strong influence on the corrosion front movement from the surface towards the substrate and therefore overall degradation of the alloy under physiological conditions changes depend on the depth of LSM region. The microstructure of the melt pool, shown figure 2(b), is found to contain an extremely fine equiaxed dendrite (enlarged view figure 2(c)) network at the top region and columnar network (enlarged view figure 2(d)) in the bottom region of the meltpool. In this highly refined zone the grain size was in the range of 1–2 μm and laser processing parameters appear to have measurable influence (table 2). The results showed that at low energy input the average grain size is slightly larger than higher energy condition. However, the grain size values are statistically not different as the variation in the grain size within the same sample is high due to the variation in the cooling rate. The grain size of the substrate was ~20 μm (figure 2(a)), which is significantly higher than that observed in LSM regions. The observed microstructural refinement is attributable to the high cooling rates associated with LSM. The coarser columnar dendritic network in figures 2(b), (d) at the bottom of the melt pool is mainly due to the reduction in solidification rate with increased melt pool depth and also due to directional heat extraction through the substrate. As the population of equiaxed cells increased at higher energy condition, this indicated that high energy density leads to temperature gradient [36]. A distinct heat affected zone (HAZ) was also seen (figure 2(d)) at the interface of the laser melted region and substrate. In the HAZ the extended network of fine cells is randomly formed and is morphologically visible. The

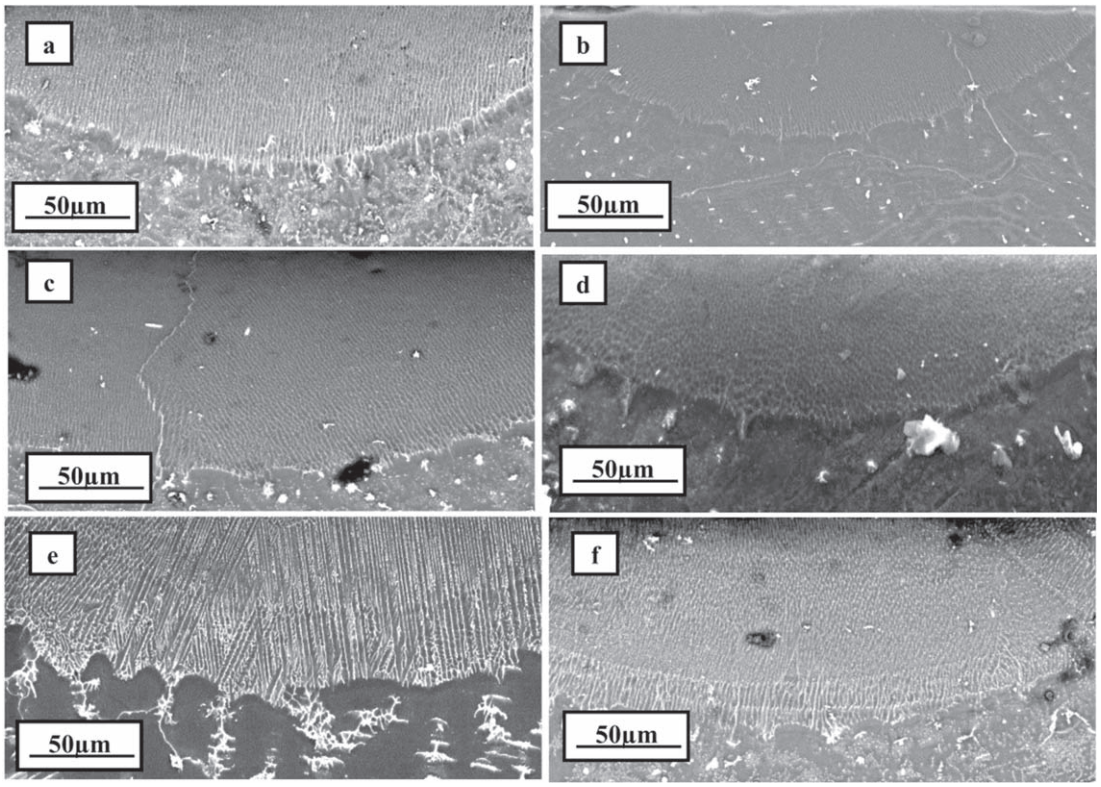

Figure 1. Cross sectional (SEM) micrograph of LSM sample with meltpool at an energy densities of (a) 12.5 J mm^{-2} (b) 17.5 J mm^{-2} (c) 22.5 J mm^{-2} (d) 25 J mm^{-2} (e) 35 J mm^{-2} (f) 45 J mm^{-2}.

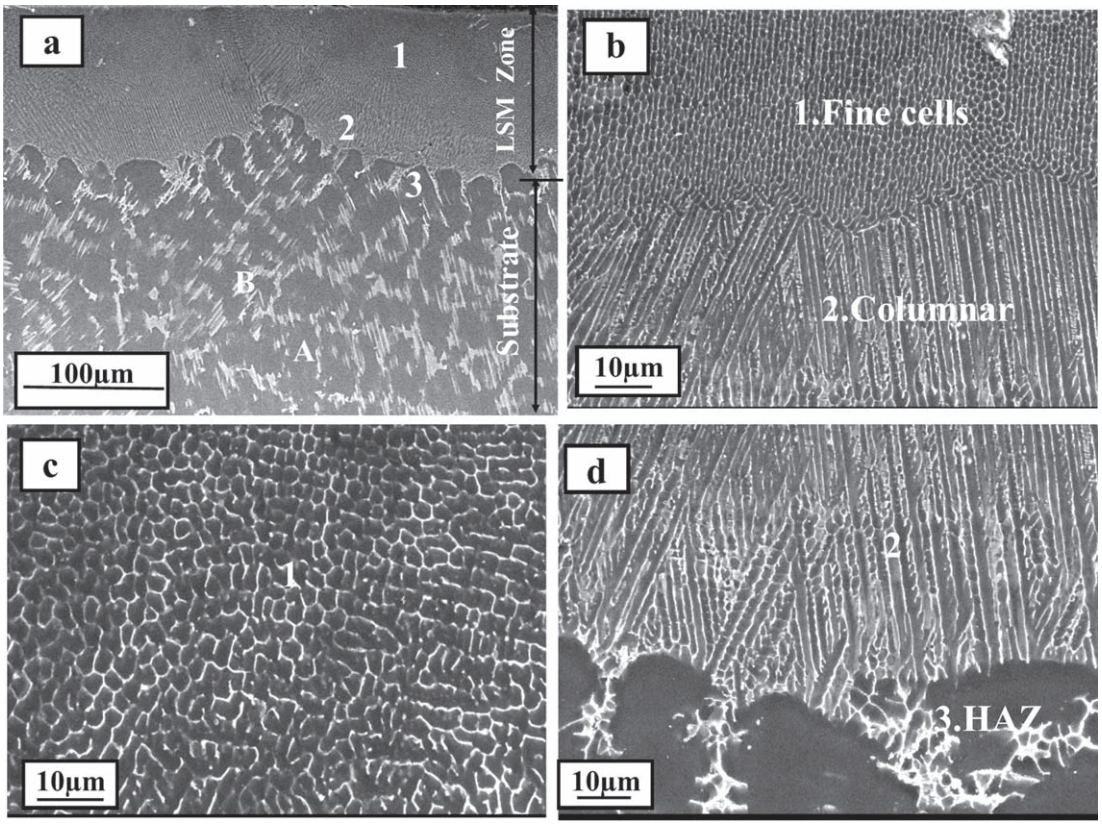

Figure 2. Typical cross sectional SEM microstructures of (a) Laser surface melted Mg-Zn-Gd alloy (b) enlarged LSM zone (at 25 J mm^{-2}) (c) Top region of the melt pool (d) Bottom region of the melt pool with heat affected zone (HAZ).

Table 2. Laser parameters used and hardness and melt pool depths of LSM Mg-Zn-Gd alloy.

Parameters (Power (W)/Velocity mm s^{-1})	Laser energy density (J mm^{-2})	Melt pool depth (μm)	Average Grain size(μm)	Roughness (S_q) (μm)
As- cast			20 ± 0.5	1.88 ± 0.1
125/20	12.5	75 ± 1	2.41 ± 0.6	4 ± 1
175/20	17.5	111 ± 3	2.34 ± 0.3	4.6 ± 0.5
225/20	22.5	138 ± 5	2.12 ± 0.5	5.3 ± 0.8
125/10	25	140 ± 3	2.01 ± 0.2	4.9 ± 1
175/10	35	148 ± 4	1.92 ± 0.5	5.8 ± 0.3
225/10	45	150 ± 5	1.73 ± 0.4	13 ± 1

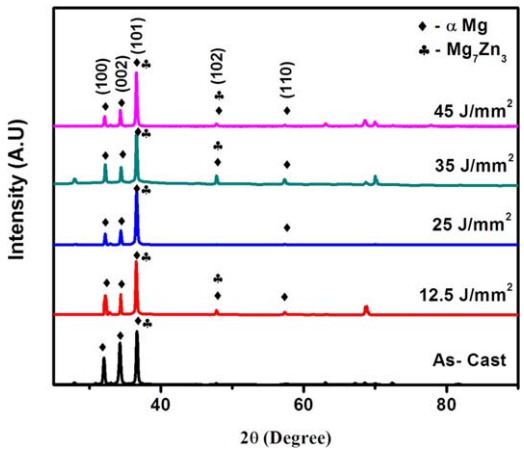

Figure 3. XRD results of as-cast and selected laser treated Mg-Zn-Gd alloy.

compositional distribution analysis by EDS shows that there is some enrichment and homogenization of Zn and Gd within the LSM region [37]. With the increasing energy density the solute enrichment in the meltpool increased too. This is evident in the combinations 45 J mm^{-2} (Zn = 2.2 ± 0.8, Gd = 2.8 ± 0.6), 12.5 J mm^{-2} (Zn = 1.8 ± 0.6, Gd = 2 ± 0.8) where the heat input resulted in enrichments of solutes in the melted region as compared to as cast alloy (table 1).

Figure 3 shows the XRD pattern of as-cast and LSM Mg-Zn-Gd alloy. The results indicate that the major peaks of all samples correspond to α-Mg phase (ICDD-PDF file no: 00-004-0770). The remaining peaks of Mg_7Zn_3 [38] indicate the secondary intermetallic phases. It is noticed that the dominating diffraction peaks at 2θ = 32.19 °, 34.4° and 36.63 ° could be assigned to (100), (002) and (101) planes of α-Mg respectively. After LSM the relative intensity of (101) increased, which suggests preferred grain orientation in the LSM region of the alloy. Some extra peaks were observed for the laser-melted sample along with the main peaks. This may be due to the change in lattice constants resulting from rapid melting and solidification which in turn leads to the formation of some intermetallic or metastable compounds [21].

3.2. Hardness, surface roughness and wettability

The influence of LSM on the surface hardness of Mg-Zn-Gd alloy is presented in figure 4. The average hardness of LSM samples ranged between 82 HV and 120 HV. The improved hardness of LSM samples is due to grain refinement and solid solution strengthening [39]. The average microhardness of laser melted alloy changed with the laser power and velocity. The samples exhibited low hardness at lower energy, density conditions (12.5 J mm^{-2}) (table 2), mainly attributable by the coarse microstructural features in the melted zone. Once the laser power increased to 17.5 J mm^{-2}, the hardness also increased as a result of formation of fine grains in the melt zone. Maximum hardness of 120 HV was observed in the samples processed at an energy density of 35 J mm^{-2}. This improvement in hardness shows that more fine grains were formed at extremely rapid cooling rates. There is a slight decrease in hardness at an energy density of 45 J mm^{-2}. The reason for this decrease may be attributed to the grain size variations with increase in scan speed.

The changes in the surface roughness of Mg-Zn-Gd alloy due to LSM are presented in table 2 and figure 5. Figure 5(a) mainly shows the typical SEM image of the laser treated surface. The selected area (white in colour) in figure 5(a) scanned for surface roughness measurement. In general, the surface roughness increased with LSM and gradual increase in the roughness was also observed with increasing laser energy density. The surface

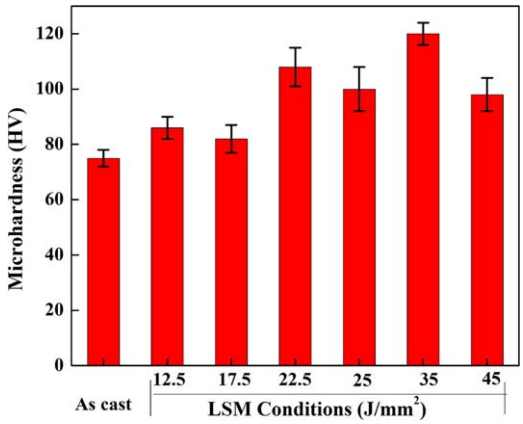

Figure 4. Hardness variation in as cast and LSM samples.

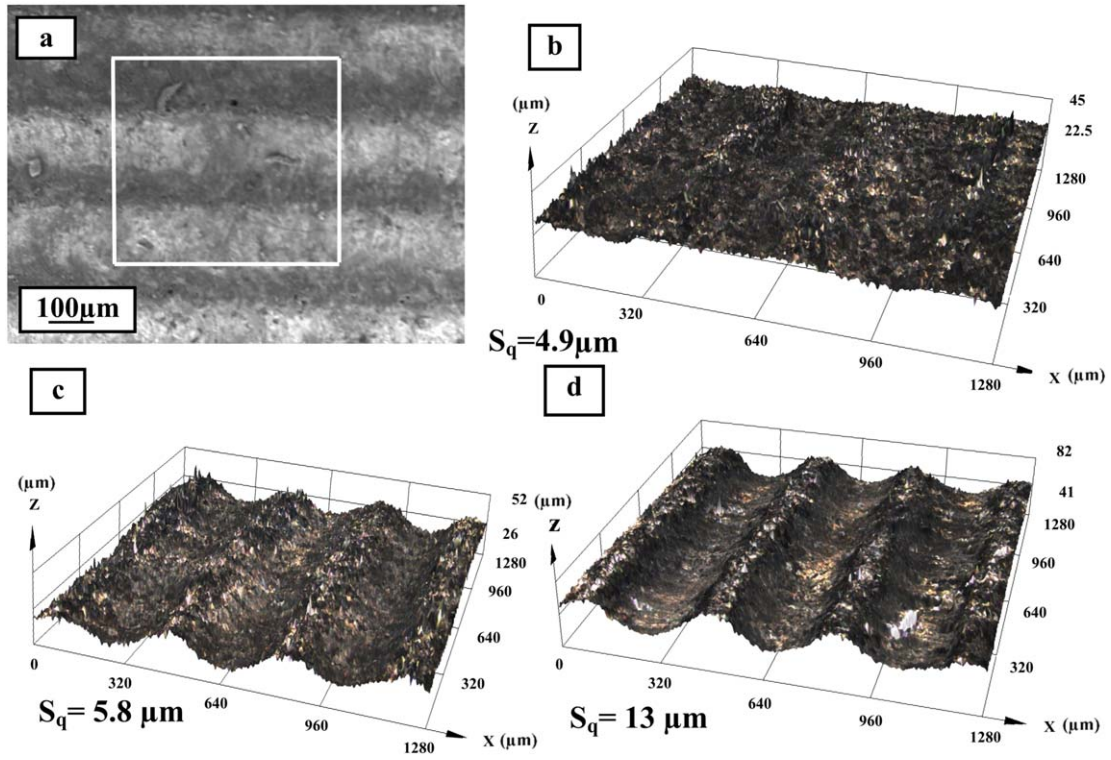

Figure 5. Surface topographies of laser treated Mg-Zn-Gd alloy (a) SEM image, Roughness (3D maps) profiles at (b) 25 (c) 35 (d) 45 J mm^{-2}.

roughness (S_q) of LSM samples ranged from 4 $\pm$ 1 μm to 13 $\pm$ 1 μm, when the laser energy density was increased from 12.5 J mm^{-2} to 45 J mm^{-2}. Various research [5, 31, 34, 35, 40, 41] has reported that recoil pressure, due to rapid heating, generates hydrodynamic melt motion inside the melt pool. These motions of the liquid metal are sufficient to eject melt towards the material interaction zone and lead to the formation of liquid pile-up. Later on the gravitational force tries to pull back the liquid metal towards the melt pool [42]. When the cooling rates are high during LSM, the liquid metal solidifies quickly, forming deep grooves and high peaks on the LSM surfaces [21]. The increase in the surface roughness with increase in the laser energy density could be due to high recoil pressure-induced shock waves at higher energy densities.

The quantitative analysis of surface wettability of LSM samples, before and after polishing, was carried out using DI water (polar). Table 3 shows the contact angles and surface energy of as-cast, LSM and polished LSM samples. Growth and adhesion of cells on the surface of the laser processed alloys are influenced by surface characteristics such as surface energy, surface roughness, surface geometry, chemical composition [22] and microstructural features such as grain size [27, 31, 36]. At low laser energy densities, the unpolished LSM sample

Table 3. Effect of LSM at different laser energy densities on the surface energy and contact angle of as cast, as-LSM and polished LSM sample.

	LSM sample		Polished LSM sample	
Parameters (J/mm^2)	Contact angle (°) DI water	Surface free energy (mN m^{-1})	Contact angle (°) DI water	Surface free energy (mN m^{-1})
As cast	90 ± 3	30 ± 6	90 ± 3	30 ± 6
12.5	72 ± 7	39.0 ± 8.3	75 ± 8	40 ± 5
17.5	79 ± 9	34.3 ± 5.6	75 ± 8	39 ± 4
22.5	83 ± 6	35.3 ± 3.7	77 ± 4	37 ± 5
25	83 ± 8	33.5 ± 5.9	80 ± 10	37 ± 3
35	91 ± 7	28.01 ± 4.9	84 ± 8	37 ± 3
45	103 ± 10	32.2 ± 3.5	89 ± 8	35 ± 2

surface was nearly hydrophilic and hence, can promote cellular adhesion. As a result, better mineralization could be achieved on these samples with low contact angles and higher surface energy [21]. As the value of contact angle increased gradually and reached 103 ± 10° with increase in the laser energy density, the surface energy of these samples was found to be low. At the highest energy density conditions (35 J mm^{-2}, 45 J mm^{-2}), the surface of the sample showed hydrophobic nature similar to as-cast samples (90 ± 3°), which can led to poor cell attachment on these samples. The changes in the solidification cooling rate as a function of laser energy density resulted in variations in the surface roughness, microstructural features and thereby altered the wettability of present samples [36]. As-cast samples with a roughness of 1.88 ± 0.1 μm and grain size of 20 ± 0.5 μm exhibited a surface energy of 30 ± 6 mN m^{-1}. However, after LSM the surface roughness of the samples increased significantly (table 2) and up to 10 times lower grain size was achieved on these samples. Further, some solute enrichment was also observed in the LSM regions (table 1). All these changes resulted in enhancement in the wettability of LSM samples. However, it is important to note that the LSM samples showed more or less similar wettability and surface energy irrespective of laser energy density. This could be due to small variations among the samples in terms of surface roughness and grain size (tables 2 and 3). Overall, the LSM samples showed relatively better wettability and surface energy than as-cast samples. However, it is not clear whether this improvement is due to changes in the surface roughness or microstructure and small composition variations due to LSM. Therefore, the wettability of samples were assessed again after polishing the samples to ensure similar surface roughness (~Sq = 1 μm) to understand the effect of microstructural and compositional changes due to LSM on wetting behavior. Since the polished samples have similar surface roughness the influence of surface roughness on wettability can be ignored. The results show (table 3) that after polishing the wettability and surface roughness of as-cast samples did not change as there is no change in the microstructure and composition in these samples after polishing. On the other hand, the wettability and surface energy of polished LSM samples showed distinguishable change, which can be attributable to the changes in the microstructure (grain refinement) and solute enrichment in LSM region, which are absent in as-cast samples. Although small, the LSM samples showed relatively better wettability than as-cast samples. The variation in the contact angle is influenced by the reduction in average grain size [36] and variations in chemical composition due solute enrichment, presence of multiple phases [31]. The EDS results confirmed that the concentration of Mg, Zn and Gd in the grains and grain boundaries vary with different laser energy densities and therefore, the grain and grain boundary interactions with a water molecule appears to be different. These results also indicate that relatively better wettability on LSM samples can be achieved after polishing, where the direct influence of grain refinement and solute enrichment was observed.

3.3. *In vitro* degradation

3.3.1. Immersion corrosion behavior

Overall degradation kinetics of laser treated Mg-Zn-Gd alloy was assessed in terms of hydrogen evolution and Mg ion release during static immersion in HBSS as represented in figure 6. All samples including as- cast alloy were fine polished and maintain a Sq of ~1 μm to eliminate the influence of surface roughness on corrosion. The measured hydrogen evolution of LSM samples compared to as-cast Mg-Zn-Gd during immersion in HBSS is represented in the figure 6(a). At all processing conditions the release of hydrogen volume increases with increase in immersion time. The same trends have been reported in AZ91D alloy also [18]. The sample processed at 125–20 (processed using lower energy density (12.5 J mm^{-2}) exhibited highest hydrogen evolution (1.35 ml cm^{-2}) suggesting its low corrosion resistance than as cast Mg-Zn-Gd. This could be mainly due to the unstable passive film formation during immersion in HBSS and the lower overlapping of meltpool (figures 8(d), (e)). The rate of hydrogen evolution was found to be high during initial ~100 h of immersion for samples treated with 12.5 J mm^{-2} and 25 J mm^{-2} laser processing conditions, which showed 1.35 ml cm^{-2} and 1.6 ml cm^{-2}

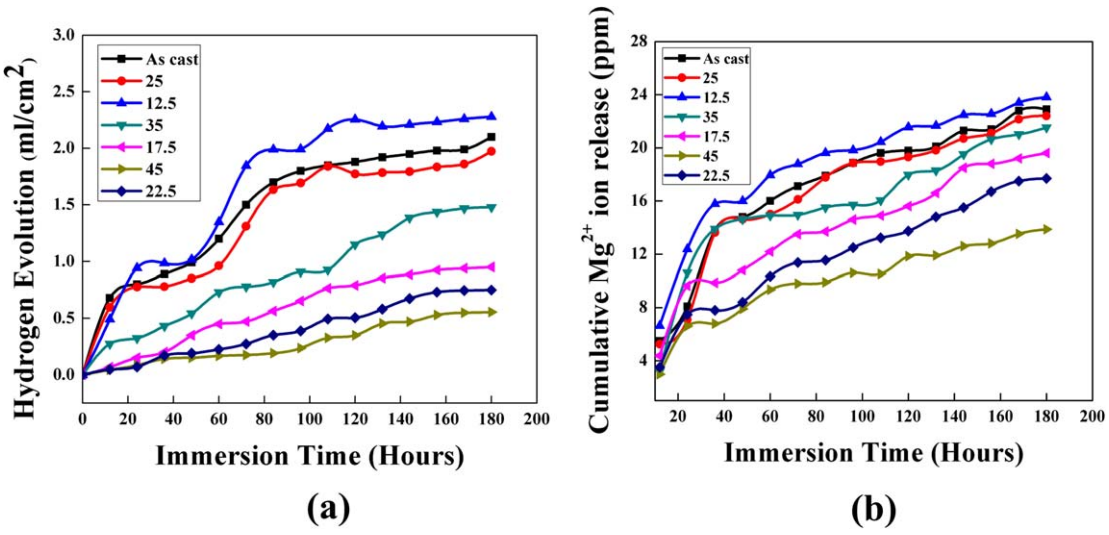

Figure 6. (a) Rate of hydrogen evolution (b) Cumulative Mg^{2+} ion release from LSM samples during immersion in HBSS (All the LSM units are in J/mm^2).

hydrogen evolution, respectively. The slope of hydrogen evolution curves was relatively low for the samples processed at high energy density and exhibited a lower corrosion rate. For example, after 140 h of immersion the hydrogen evolution almost became stable for samples treated at 45 J mm^{-2}, 35 J mm^{-2} and 22.5 J mm^{-2}. Among all the processing conditions 45 J mm^{-2} had higher corrosion resistance with lowest hydrogen evolution could be due to a persistent stable passive film on its surface. At higher energy densities, which will try to further inhibit corrosion propagation. The range of passivation is better in these conditions by the linear polarization study which is explained later in this work. The rate of hydrogen evolution up to 100 h (slope of hydrogen evolution versus time) for 45 J mm^{-2} also shows a lower value 0.0024 ml cm^{-2} h^{-1} compared to 12.5 J mm^{-2} (0.02 ml cm^{-2} h^{-1}) and as-cast (0.16 ml cm^{-2} h^{-1}) conditions. Similarly, the hydrogen evolution at 22.5 J mm^{-2} is 0.006 ml cm^{-2} h^{-1} which is very much lower than the 0.29 ml cm^{-2} h^{-1} measured at 35 J mm^{-2} condition.

The anodic reaction of Mg results in the formation of Mg^{2+} ions and therefore, analysis of Mg^{2+} ion release during immersion can give extent of alloy degradation. Figure 6(b) shows the cumulative Mg^{2+} ion release of different samples as a function of immersion time, the ion release trend was found to be in line with the hydrogen evolution trend. There is a sharp increase in ion release during the initial 20 h of immersion for all processed samples. This could be mainly due to high rate of anodic dissolution. Samples processed at 225/10 (higher energy density-45 J mm^{-2}) showed lower ion release (13.9 ppm) which matches the trend of the hydrogen evolution plot. This lower ion release could be due to the stability of the passive film which is formed and persistent after 140 h of immersion. As compared to the as cast samples there is strong reduction (~130%) in Mg^{2+}ions release for sample processed at higher laser energy condition. The maximum possible Mg^{2+} release of 23 ppm was observed for 12.5 J mm^{-2} condition with maximum damage on the surface as well as cross section (figures 8(b), 9(a))

The highly reactive nature of Mg causes fast surface corrosion. Hence it is essential to provide for a thicker LSM layer for extended corrosion protection. The corrosion rate of different samples, calculated using the weight loss method, is summarized in figure 7. The *in vitro* degrdation rates of LSM samples after surface polishing were found to match very well the hydrogen evolution and Mg^{2+} ion release data. The data clearly showed that LSM decreases the corrosion rate of Mg-Zn-Gd alloy. The corrosion rate of laser processed sample decreased by 53% for 45 J mm^{-2} samples compared to as-cast alloy. The decrease in trend could be due to the reduction in active ionic concentration and the reduction of any oxide layer which is formed during LSM. At high power and scan velocities of 10 mm s^{-1} and 20 mm s^{-1}, the corrosion rate decreased due to the homogenous chemical composition, higher enrichment of Zn and Gd in the melt zone and enhanced melt pool depth. This prolongs to the corrosion front propagation to reach the melt pool boundary. The samples processed at low laser power (125 W) showed no improvement in corrosion resistance owing to solidification crack, insufficient melt pool track overlapping and shallow meltpool depth (figures 8(d), (e)). The corrosion in the current LSM Mg-Zn-Gd alloy is mainly due to the active ions present at the laser track, corrosion due to the formation of galvanic cell between α-Mg and secondary phases (between the remelted and unmelted region of the alloy). Once the corrosion starts, the propagation of corrosion front presumed to advance due to (i) the corrosion potential between the meltpool, meltpool boundary and the substrate (ii) differences in internal stress

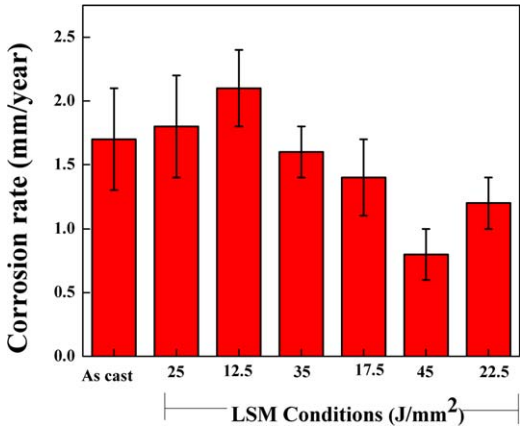

Figure 7. Corrosion rate of as cast and LSM samples by weight loss after 180 h immersion in HBSS.

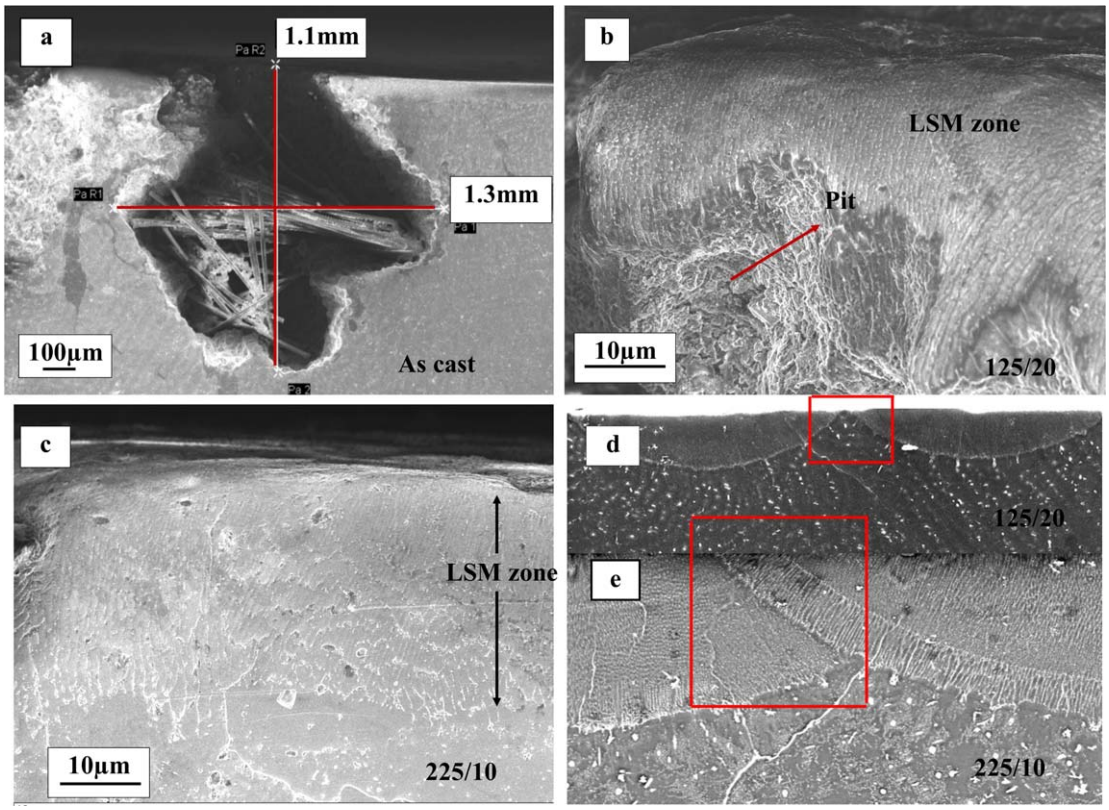

Figure 8. Cross sectional view of the corroded surface after the immersion in HBSS for 180 h(a) As- cast Mg-Zn-Gd alloy and laser treated at (b) 12.5 J mm^{-2} (c) 45 J mm^{-2} and meltpool overlapping variations at (d)12.5 J mm^{-2} (e) 45 J mm^{-2}.

between substrate and meltpool, which could initiate stress corrosion. Therefore samples with a low melt pool depth samples would experience higher degradation rates. In meltpool region of LSM, equiaxed and fine grains with or without secondary phases at the grain boundaries and extended enhanced solid solubility of alloying element leads to increased corrosion resistance [38, 39, 43]. Moreover, suitable melt depth is required to make use of such benefits in the long time corrosion tests. However the results shows that 25 J mm^{-2} and 12.5 J mm^{-2} samples have the corrosion rates of 1.8 $\pm$ 0.4 and 2.1 $\pm$ 0.3 mmpy which is higher than that of as-cast Mg-Zn-Gd (1.7 $\pm$ 0.4 mmpy) mainly due to their shallow meltpool depth with lower overlapping and possible presence of cracks (figures 8(d), (e) [44]. At high heat input resulted enrichment of solute atoms in α-Mg matrix increased the resistance against the pitting corrosion [45]. When compared to 45 J mm^{-2} (0.8 $\pm$ 0.2 mmpy) and 22.5 J mm^{-2} (1.2 $\pm$ 0.2 mmpy) conditions as-cast Mg-Zn-Gd alloy (1.7 $\pm$ 0.4 mmpy) shows no higher enrichment of solute atoms leads to lower resistance to pitting mode of corrosion.

Table 4. Corrosion and statistical analysis results of samples after 180 h of immersion.

Laser processing parameters (J mm^{-2})	Corrosion rate by weight loss (mm/year)	P values
25	1.8 ± 0.4	0.021
12.5	2.1 ± 0.3	0.062
35	1.6 ± 0.2	0.385
17.5	1.4 ± 0.3	0.098
45	0.8 ± 0.2	0.004
22.5	1.2 ± 0.2	0.004

To determine the depth of corrosion penetration and its correlation with meltpool depth, the microstructure of cross sectional samples of as-cast, 12.5 J mm^{-2} and 45 J mm^{-2} samples after 180 h of immersion were studied with SEM. The corroded area extended deeply into the interior and formed a pit of 1.3 mm width and 1.1 mm depth in as-cast Mg-Zn-Gd alloy. The 12.5 J mm^{-2} LSM samples showed that the melt pool tracks did not significantly overlap (figure 8(d)). This will lead to the faster corrosion propagation through the interface of the two successive laser scans. Figure 8(d) shows that corrosion front slowly moves through the substrate by crossing the melt pool region. Owing to the difference in the anodic and cathodic ratio between the substrate and meltpool boundary, many corrosion sites will form. These corrosion sites will further lead to pit formation (figure 8(b)). However, for samples treated at 45 J mm^{-2} conditions figures 8(c), (e) increased overlapping of meltpool and enhanced meltpool depth prolonged long term corrosion rate without visible penetration of corrosion thus, indicating their superior corrosion resistance.

Statistical analysis on corrosion rate by weight loss method with respect to the as cast condition was carried out by considering alpha (α) value of 5% and the results are shown in table 4 with p values. These results indicate that at a laser energy density of 35 J mm^{-2} the corrosion rate is considered to be not statistically significant compared to all other processing conditions where the corrosion rates are either statistically significant or nearly statistically significant.

To gain improved understanding of the mechanism of corrosion, powder scrapped off the corroded sample surfaces (25 and 12.5 J mm^{-2}) were examined by XRD and SEM + EDS. Figures 9(a)–(c) show the SEM micrographs of top surface of laser melted samples after immersion in HBSS for 180 h. It is observed that the entire surface has undergone localized corrosion.

The SEM images show a porous layer covering the entire surface of the samples. Some samples also exhibited cracks on the surface (figure 9(b)). When Mg alloy specimen are exposed to HBSS, the anodic reaction resulted in increased Mg^{2+} dissolution and the presence of Cl^- concentration in the solution [46]. The presence of aggressive Cl^- transform the passive film Mg $(OH)_2$ into more soluble $MgCl_2$. This breakdown of Mg $(OH)_2$ reduces the protected area, finally promoting further corrosion of substrate [47]. The formation of Mg $(OH)_2$ was confirmed by XRD analysis shown in figure 9(d). At low laser power and velocity (figure 9(a)), the corroded surface revealed a film with large size pits and increased corrosion products. On the other hand, the samples processed at high laser power and scan velocity (figure 9(c)), the amount of corrosion products was noticeably reduced less with isolated regions of loosely bound corrosion products. A crack, visible on the surface of corrode sample 35 J mm^{-2} is shown in figure 9(b). This indicates that the oxide films became porous and starts to peel off from the surface during long-term immersion in HBSS. The passive film of $Mg(OH)_2$ is more stable and further movement of corrosion front towards the substrate can be impeded by this layer.

A typical XRD spectrum of corroded surface is presented in figure 9(d). The XRD results confirms the formation of HAp (ICDD-PDF file no: 00-009-0432), $Mg(OH)_2$ (ICDD-PDF file no: 00-044-1482) and $Ca_3(PO_4)$ (ICDD-PDF file no: 00-009-0348). After immersion in HBSS for 180 h. Figure 9(a.1) indicates the formation of flower like structure [48]. The EDS analysis of these products showed the presence of Ca, P, O and Mg suggesting the formation of apatite which will support bone healing [44]. The surface layer also quantifies the Mg and O atomic ratio of 1:2, that implies the presence of $Mg(OH)_2$ [49]. The emerged $Mg(OH)_2$ film with different layer density favors the effective corrosion protection by slowing down the Mg dissolution. Therefore considerable amounts of $Mg(OH)_2$ precipitated on the laser melted surface may act as a protection by preventing the direct contact with HBSS.

3.3.2. Electrochemical corrosion behavior

The corrosion current density (i_{corr}) and corresponding corrosion potential (E_{corr}) derived from Tafel extrapolation curves and are summarized in table 5. The results suggest that as-cast Mg-Zn-Gd alloy has a more negative potential (−1.56 ± 0.3 V v/s SCE) than the LSM samples. The corrosion potential (E_{corr}) of LSM at 45 J mm^{-2} and 22.5 J mm^{-2} were −1.36 ± 0.03 V v/s SCE, −1.32 ± 0.04 V v/s SCE, which is relatively nobler

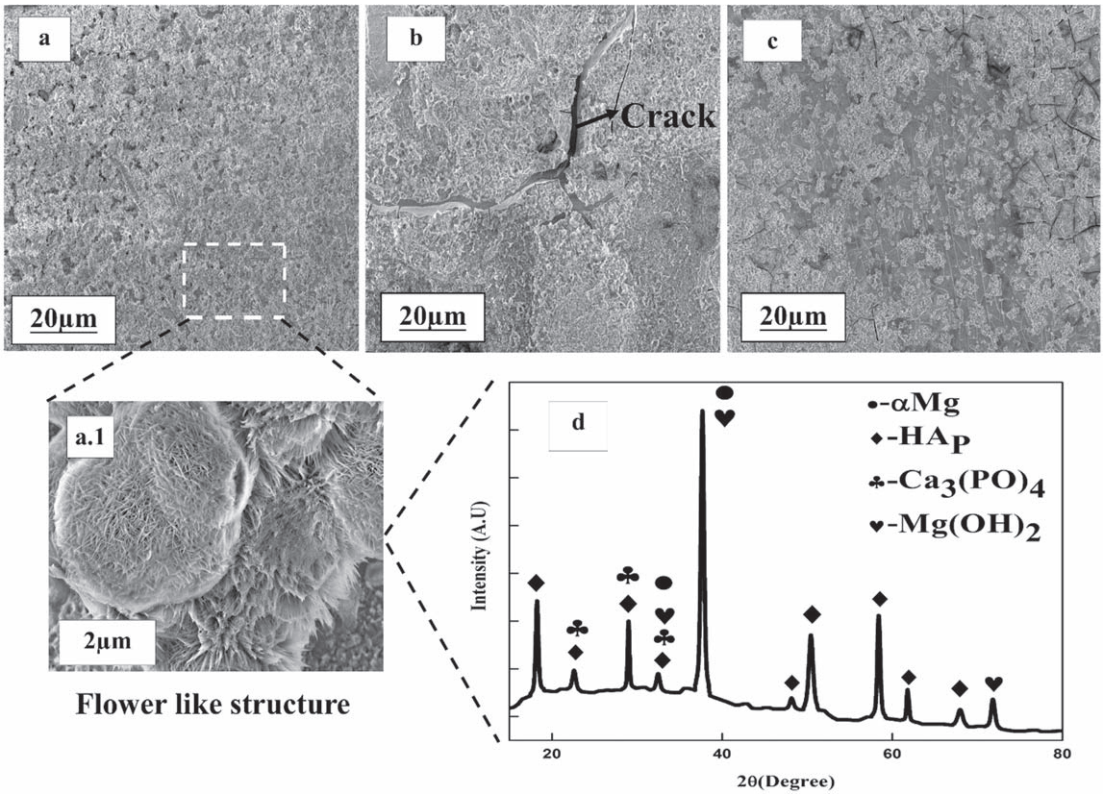

Figure 9. Surface morphology of degraded Mg-Zn-Gd alloy (a) 12.5 J mm^{-2} (b) (a.1) Enlarged view of the surface product (b) 35 J mm^{-2} (c) 45 J mm^{-2} (d) XRD spectra of corrosion product extracted from 25 J mm^{-2} laser melted sample immersed in HBSS for 180 h.

Table 5. Electrochemical parameters and corrosion rates determined using electrochemical and weight loss method.

	Plot extrapolation		
Parameters (J mm^{-2})	E_{corr} (V versus SCE)	i_{corr} (mA cm^{-2})	Corrosion rate (mm/year)
As-cast	−1.56 ± 0.3	0.008 ± 0.5	0.41 ± 0.15
25	−1.53 ± 0.1	0.0051 ± 0.04	0.13 ± 0.08
12.5	−1.48 ± 0.07	0.0024 ± 0.04	0.29 ± 0.13
35	−1.44 ± 0.02	0.0026 ± 0.03	0.08 ± 0.05
17.5	−1.43 ± 0.06	0.0023 ± 0.02	0.07 ± 0.2
45	−1.36 ± 0.03	0.0021 ± 0.01	0.06 ± 0.1
22.5	−1.32 ± 0.04	0.0013 ± 0.02	0.07 ± 0.2

than material processed at 25 J mm^{-2} (−1.53 ± 0.1 V v/s SCE) and as cast system. But there is no large difference in E_{corr} value between as cast and LSM at 25 J mm^{-2} condition. Moderate range of potential −1.44 ± 0.02 V v/s SCE and −1.43 ± 0.06 V v/s SCE were exhibited LSM at 35 J mm^{-2} and 17.5 J mm^{-2}. From the results of corrosion current density, it appears that corrosion current i_{corr} decreases marginally with respect to the change in power and velocity. LSM sample at 45 J mm^{-2} shows a lower value of i_{corr} 0.0013 ± 0.02 mA cm^{-2} as compared to as cast 0.008 ± 0.5 mA cm^{-2}. The trends of the electrochemical corrosion test and weight loss method agrees with each other. However, the corrosion rate measured by the weight loss method were always higher than that rate obtained from the electrochemical measurement due to the following reasons [50, 51]. Measurement of corrosion rate by Tafel plot is fundamentally an instantaneous technique where measurement can be taken for a particular time. But in the case of magnesium alloys, corrosion is not constant with time in solution. Typically corrosion initially starts at localized regions and after a period of immersion it slowly expand over the surface. In this aspects weight loss measurement record the average values of corrosion rate over the period of immersion. This mainly shows that a short term test requires stringent

evaluation of Tafel extrapolation under condition that gives a measurement that is comparable to immersion studies

The improved corrosion resistance of laser treated alloy at 225/10 (45 J mm^{-2}) is attributed to the formation of protective hydroxide film ($Mg(OH)_2$) on these samples. In as-cast Mg-Zn-Gd alloy the formation of oxide film starts at the region adjacent to grain boundary adjacent region and further move towards the interior [20]. The precipitated fine intermetallic phase in Mg-Zn-Gd [35] laser melted samples along the grain boundary act as a cathode to the grain. At the initial stages of corrosion grain boundary precipitates remain unaffected. Later on, corrosion initiates from the matrix-precipitate interface. Hence the galvanic couple effect between grain and grain boundary leads in time to the increase in corrosion attack on the grain. The large anode to cathode ratio of the precipitate phase noticeably influences the corrosion performance of the alloy system. In this regard, LSM positively influences the corrosion resistance by making a significant change in grain refinement and redistribution of precipitates along the grain boundary. Formation of smaller grains results in higher grain boundary areas and therefore more precipitates along the grain boundaries, which decreases the cathode to anode area ratio. This result in a decrease in the corrosion rate of LSM samples. In this study the alloy processed with higher laser power conditions (225/10 and 225/20) showed comparatively lower corrosion rate than as cast Mg-Zn-Gd alloy (table 5). This could be mainly due to better fraction of grain size reduction as compared with the lower power condition and the barrier effect of secondary phase (Mg_3Gd) [52] in Mg-Zn-Gd alloy. Also during melting, rapid heating and cooling leads to the increase in the alloying element concentration which is present in the solid solution [15] and provides a passive behavior to the melted surface. Higher corrosion rate of 0.41 mm/year and 0.31 mm/year were observed at 25 J mm^{-2} and 12.5 J mm^{-2} processing conditions were mainly due to the lower grain refinement zone (melt pool). As it is seen in the cross sectional image (figures 8(b), (d)) the lower overlapping percentage between the melt pool acts as a corrosion initiation sites. When the samples exposed to HBSS (same mechanism has observed during immersion corrosion study), the chloride ion present in the electrolyte entrapped to these corrosion sites and further damages the passive film ($Mg(OH)_2$). Later on the exposed area undergoes self-dissolution and thereby corrosion rate has increased largely. On the other hand moderate corrosion resistance which was observed for 175 W power and 20 mm s^{-1} scan velocity. At this condition the passive film which is formed on the LSM surface is comparatively stable due to the grain boundary anchoring effect for small interval of time [20]. As compared to the untreated Mg-Zn-Gd alloy LSM samples showed maximum of 82% enhancement in corrosion resistance for 45 J mm^{-2}. The as cast Mg-Zn-Gd alloy mainly consist of coarse grain α-Mg and Mg_3Gd phase. The non-uniform and bigger sized secondary phase distributed in the α-Mg grain boundaries act as a galvanic couple with the matrix [53]. The increased in cathodic to anodic area ratio further promotes the corrosion movement by breaking the barrier film and finally leads to higher corrosion rate (0.41 mm/year).

The study reveals that surface properties such as wettability, biodegradation of developed Mg-Zn-Gd alloy was tailored effectively by LSM. Controlling the laser process parameters such as laser power and scan speed also controls the melt pool depth, surface roughness and crack density. Consequently these properties must be tailored to ensure the effective use of prepared alloy for temporary implant application.

4. Conclusions

The effect laser surface melting with different power and scan velocities on microstructure, mechanical properties, surface energy and degradation properties of Mg-Zn-Gd alloy was investigated. Based on the results following conclusions were drawn.

1. Grain refinement and high degree of homogenization was observed due to LSM and is attributed to the rapid cooling rates associated with laser processing. The meltpool depth increased with increasing the laser energy density.
2. LSM generates a rougher surface texture of the Mg alloy. The surface became rougher with increasing energy densities. Due to the rapid melting and vaporization, the induced recoil pressure at the laser material interaction zone generate high velocity melt flow, leading to the deeper valleys and peaks.
3. The LSM samples exhibited improved wettability compared to as-cast alloy when treated with low energy density. A maximum surface energy of 40 $\pm$ 5 mN m^{-1} was obtained for polished samples with lowest contact angle of 75 $\pm$ 8°, which is expected to facilitate cell adhesion, proliferation and bio-mineralization on LSM-treated alloy surfaces.
4. *In vitro* degradation evaluation by immersion and electrochemical studies showed clear improvement in corrosion resistance due to LSM. When the alloy was treated at 45 J mm^{-2} the corrosion resistance increased by 53%.

Acknowledgments

The authors would like to thank the Department of Metallurgical and Materials Engineering, and the Department of Chemical Engineering, National Institute of Technology, Karnataka for providing access to various experimental facilities.

ORCID iDs

Srikanth Bontha https://orcid.org/0000-0002-8803-6774
Ramesh M R https://orcid.org/0000-0003-2280-1995

References

[1] Chen Y, Xu Z, Smith C and Sankar J 2014 Recent advances on the development of magnesium alloys for biodegradable implants *Acta Biomater.* **10** 4561–73
[2] Staiger M P, Pietak A M, Huadmai J and Dias G 2006 Magnesium and its alloys as orthopedic biomaterials: a review *Biomaterials* **27** 1728–34
[3] Kainer K U, Bala Srinivasan P, Blawert C and Dietzel W 2010 Corrosion of magnesium and its alloys *Shreir's Corros.* **51** 2011–41
[4] Li Z, Gu X, Lou S and Zheng Y 2008 The development of binary Mg-Ca alloys for use as biodegradable materials within bone *Biomaterials* **29** 1329–44
[5] Liu C, Xin Y, Tang G and Chu P K 2007 Influence of heat treatment on degradation behavior of bio-degradable die-cast AZ63 magnesium alloy in simulated body fluid *Mater. Sci. Eng.* A **456** 350–7
[6] Witte F, Fischer J, Nellesen J, Crostack H A, Kaese V, Pisch A, Beckmann F and Windhagen H 2006 *In vitro* and *in vivo* corrosion measurements of magnesium alloys *Biomaterials* **27** 1013–8
[7] Witte F, Kaese V, Haferkamp H, Switzer E, Meyer-Lindenberg A, Wirth C J and Windhagen H 2005 *In vivo* corrosion of four magnesium alloys and the associated bone response *Biomaterials* **26** 3557–63
[8] Song Y, Shan D, Chen R, Zhang F and Han E H 2009 Biodegradable behaviors of AZ31 magnesium alloy in simulated body fluid *Mater. Sci. Eng.* C **29** 1039–45
[9] Feyerabend F, Fischer J, Holtz J, Witte F, Willumeit R, Drücker H, Vogt C and Hort N 2010 Evaluation of short-term effects of rare earth and other elements used in magnesium alloys on primary cells and cell lines *Acta Biomater.* **6** 1834–42
[10] Leng Z, Zhang J, Zhang M, Liu X, Zhan H and Wu R 2012 Microstructure and high mechanical properties of Mg-9RY-4Zn (RY: Y-rich misch metal) alloy with long period stacking ordered phase *Mater. Sci. Eng.* A **540** 38–45
[11] Gray J E and Luan B 2002 Protective coatings on magnesium and its alloys — a critical review *J. Alloys Compd.* **336** 88–113
[12] Liu C, Liang J, Zhou J, Wang L and Li Q 2015 Effect of laser surface melting on microstructure and corrosion characteristics of AM60B magnesium alloy *Appl. Surf. Sci.* **343** 133–40
[13] Guo L F, Yue T M and Man H C 2005 Excimer laser surface treatment of magnesium alloy WE43 for *J. Mater. Sci.* **40** 3531–3
[14] Wang L, Zhou J, Liang J and Chen J 2012 Microstructure and corrosion behavior of plasma electrolytic oxidation coated magnesium alloy pre-treated by laser surface melting *Surf. Coatings Technol.* **206** 3109–15
[15] Abbas G, Liu Z and Skeldon P 2005 Corrosion behaviour of laser-melted magnesium alloys *Appl. Surf. Sci.* **247** 347–53
[16] Dubé D, Fiset M, Couture A and Nakatsugawa I 2001 Characterization and performance of laser melted AZ91D and AM60B *Mater. Sci. Eng.* A **299** 38–45
[17] Taltavull C, Torres B, López A J, Rodrigo P and Rams J 2013 Surface & coatings technology novel laser surface treatments on AZ91 magnesium alloy *Surf. Coat. Technol.* **222** 118–27
[18] Taltavull C, Torres B, Lopez A J, Rodrigo P, Otero E, Atrens A and Rams J 2014 Corrosion behaviour of laser surface melted magnesium alloy AZ91D *Mater. Des.* **57** 40–50
[19] Banerjee P C, Raman R K S, Durandet Y and McAdam G 2011 Electrochemical investigation of the influence of laser surface melting on the microstructure and corrosion behaviour of ZE41 magnesium alloy—an EIS based study *Corros. Sci.* **53** 1505–14
[20] Dutta Majumdar J, Galun R, Mordike B L and Manna I 2003 Effect of laser surface melting on corrosion and wear resistance of a commercial magnesium alloy *Mater. Sci. Eng.* A **361** 119–29
[21] Ho Y-H, Vora H D and Dahotre N B 2015 Laser surface modification of AZ31B Mg alloy for bio-wettability *J. Biomater. Appl.* **29** 915–28
[22] Rosales-Leal J I, Rodríguez-Valverde M A, Mazzaglia G, Ramón-Torregrosa P J, Díaz-Rodríguez L, García-Martínez O, Vallecillo-Capilla M, Ruiz C and Cabrerizo-Vílchez M A 2010 Effect of roughness, wettability and morphology of engineered titanium surfaces on osteoblast-like cell adhesion *Colloids Surfaces A Physicochem. Eng. Asp.* **365** 222–9
[23] Rupp F, Scheideler L, Rehbein D, Axmann D and Geis-Gerstorfer J 2004 Roughness induced dynamic changes of wettability of acid etched titanium implant modifications *Biomaterials* **25** 1429–38
[24] Guan Y C, Zhou W, Li Z L and Zheng H Y 2013 Femtosecond laser-induced iridescent effect on AZ31B magnesium alloy surface *J. Phys. D: Appl. Phys.* **46** 425305
[25] Furlan V, Demir A G and Previtali B 2015 Micro and sub-micron surface structuring of AZ31 by laser re-melting and dimpling *Opt. Laser Technol.* **75** 164–72
[26] Dean D D 1996 Surface roughness modulates the local production of growth factors and cytokines by osteoblast-like MG-63 cells *J. Biomed.Mater.Res.* **32** 55–63
[27] Demir A G, Furlan V, Lecis N and Previtali B 2014 Laser surface structuring of AZ31 Mg alloy for controlled wettability *Biointerphases* **9** 029009
[28] Janssen M I, Van Leeuwen M B M, Van Kooten T G, De Vries J, Dijkhuizen L and Wösten H A B 2004 Promotion of fibroblast activity by coating with hydrophobins in the β-sheet end state *Biomaterials* **25** 2731–9
[29] Baier R E 2006 Surface behaviour of biomaterials: the theta surface for biocompatibility *J. Mater. Sci., Mater. Med.* **17** 1057–62
[30] Gökhan A, Taketa T B, Tolouei R, Furlan V, Paternoster C, Beppu M M, Mantovani D and Previtali B 2015 Laser surface structuring affects polymer deposition, coating homogeneity, and degradation rate of Mg alloys *Mater. Lett.* **160** 359–62

[31] Kurella A K, Hu M Z and Dahotre N B 2008 Effect of microstructural evolution on wettability of laser coated calcium phosphate on titanium alloy *Mater. Sci. Eng.* C **28** 1560–4
[32] Owens D K and Wendt R C 1969 Estimation of the surface free energy of polymers *J. Appl. Polym. Sci.* **13** 1741–7
[33] Song G, Atrens A and StJohn D 2013 An hydrogen evolution method for the estimation of the corrosion rate of magnesium alloys *Magnes. Technol.* **2001** 254–62
[34] Cor E 2004 Standard practice for laboratory immersion corrosion testing of metals 1 *Corrosion* **72** 1–8
[35] Srinivasan A, Huang Y, Mendis C L, Blawert C, Kainer K U and Hort N 2014 Investigations on microstructures, mechanical and corrosion properties of Mg-Gd-Zn alloys *Mater. Sci. Eng.* A **595** 224–34
[36] Ho Y H, Vora H D and Dahotre N B 2015 Laser surface modification of AZ31B-Mg alloy for bio-wettability *J. Biomater. Appl.* **29** 915–28
[37] Manne B, Thiruvayapati H, Bontha S, Motagondanahalli Rangarasaiah R, Das M and Balla V K 2018 Surface design of Mg-Zn alloy temporary orthopaedic implants: tailoring wettability and biodegradability using laser surface melting *Surf. Coatings Technol.* **347** 337–49
[38] Datta M K, Chou D T, Hong D, Saha P, Chung S J, Lee B, Sirinterlikci A, Ramanathan M, Roy A and Kumta P N 2011 Structure and thermal stability of biodegradable Mg-Zn-Ca based amorphous alloys synthesized by mechanical alloying *Mater. Sci. Eng. B Solid-State Mater. Adv. Technol.* **176** 1637–43
[39] Wei K, Gao M, Wang Z and Zeng X 2014 Effect of energy input on formability, microstructure and mechanical properties of selective laser melted AZ91D magnesium alloy *Mater. Sci. Eng.* A **611** 212–22
[40] Samant A N and Dahotre N B 2009 Laser machining of structural ceramics-a review *J. Eur. Ceram. Soc.* **29** 969–93
[41] Vora H D, Santhanakrishnan S, Harimkar S P, Boetcher S K S and Dahotre N B 2013 One-dimensional multipulse laser machining of structural alumina: evolution of surface topography *Int. J. Adv. Manuf. Technol.* **68** 69–83
[42] Semak V and Matsunawa A 1999 The role of recoil pressure in energy balance during laser materials processing *J. Phys. D: Appl. Phys.* **30** 2541–52
[43] Vora H D, Santhanakrishnan S, Harimkar S P, Boetcher S K S and Dahotre N B 2012 Evolution of surface topography in one-dimensional laser machining of structural alumina *J. Eur. Ceram. Soc.* **32** 4205–18
[44] Guan Y C, Zhou W and Zheng H Y 2009 Effect of laser surface melting on corrosion behaviour of AZ91D Mg alloy in simulated-modified body fluid *J. Appl. Electrochem.* **39** 1457–64
[45] Coy A E, Viejo F, Garcia-Garcia F J, Liu Z, Skeldon P and Thompson G E 2010 Effect of excimer laser surface melting on the microstructure and corrosion performance of the die cast AZ91D magnesium alloy *Corros. Sci.* **52** 387–97
[46] Yang M, Cheng L and Pan F 2009 Comparison about effects of Ce, Sn and Gd additions on as-cast microstructure and mechanical properties of Mg-3.8Zn-2.2Ca (wt%) magnesium alloy *J. Mater. Sci.* **44** 4577–86
[47] Xin Y, Hu T and Chu P K 2011 *In vitro* studies of biomedical magnesium alloys in a simulated physiological environment: a review *Acta Biomater.* **7** 1452–9
[48] Nge T, Sugiyama J and Bulone V 2010 Bacterial cellulose-based biomimetic composites *Biopolymers* (Rijeka: Intech) (https://doi.org/10.5772/10269)
[49] Lei T, Tang W, Cai S H, Feng F F and Li N F 2012 On the corrosion behaviour of newly developed biodegradable Mg-based metal matrix composites produced by *in situ* reaction *Corros. Sci.* **54** 270–7
[50] Shi Z, Liu M and Atrens A 2010 Measurement of the corrosion rate of magnesium alloys using Tafel extrapolation *Corros. Sci.* **52** 579–88
[51] Song G and Atrens A 2003 Understanding magnesium corrosion—a framework for improved alloy performance *Adv. Eng. Mater.* **5** 837–58
[52] Yamasaki M, Sasaki M, Nishijima M, Hiraga K and Kawamura Y 2007 Formation of 14H long period stacking ordered structure and profuse stacking faults in Mg-Zn-Gd alloys during isothermal aging at high temperature *Acta Mater.* **55** 6798–805
[53] Zhou J, Xu J, Huang S, Hu Z, Meng X and Feng X 2017 Effect of laser surface melting with alternating magnetic field on wear and corrosion resistance of magnesium alloy *Surf. Coatings Technol.* **309** 212–9
[54] Paital S R and Dahotre N B 2009 Wettability and kinetics of hydroxyapatite precipitation on a laser-textured Ca-P bioceramic coating *Acta Biomater.* **5** 2763–72